Near Infrared In-situ Measurements for the Detection of Keyhole Porosity in Autogenous Ti-6Al-4V Welds

Joseph N. Zalameda[1], Samuel J. A. Hocker[1], Peter W. Spaeth[1] and Brandon Widener[2]

[1]NASA Langley Research Center, Hampton, VA 23681-2199
[2]Analytical Mechanics Associates, Hampton, VA 23666

ABSTRACT

Certification of additive manufactured metal parts requires nondestructive evaluation (NDE) to ensure build quality. NDE can be performed during the build process or post build. For large parts with complex geometries, post build NDE can be challenging. In-situ NDE potentially provides a way to perform the inspection layer by layer. This work explores the use of a high speed near infrared (NIR) camera that is focused in-line with a laser to obtain high spatial and temporal resolution thermal imagery of the melt pool and associated cooling areas. The thermal data is obtained during a laser melting process using a Ti-6Al-4V plate and of particular interest is the detection of keyhole porosity. Keyhole porosity can result from non-optimal build conditions, such as excessive laser power at a given laser scanning speed, that creates an entrapped bubble. The NIR measured melt pool and cooling areas are processed to detect keyhole porosity. The results are compared to X-ray computed tomography (CT) for validation. Keyhole pores buried deep were not detectable with this technique, however, some larger subsurface elongated pores and some open surface pores did show some promise for detectability.

Keywords: additive manufacturing, keyhole porosity, in-situ near infrared imaging, laser co-axial near infrared measurements, melt pool imaging, X-ray computed tomography

1. INTRODUCTION

Additively manufactured (AM) metal parts, built using laser powder bed fusion, is growing in aerospace applications. The advantages are that complex shapes and intricate internal geometries can be rapidly built. If these structures are to be used in primary load applications, they must be certified. The certification process will involve build quality assessment using nondestructive evaluation (NDE). NDE can be applied both during the build process (in-situ inspection) and post build (ex-situ inspection). Both inspection methodologies are required, however, in-situ inspection offers some advantages such as the potential to detect defects during the build layer by layer. If a significant defect is detected the build can be stopped to avoid wasting material and time. If repairable defects are detected, then processing measures can be employed to correct the defects and continue the build. In-situ NDE can therefore provide a capability that can reduce both build time and cost while ensuring improved part quality.

Defects such as lack of fusion and keyhole porosity are understood to have a strong correlation with processing conditions [1,2]. These defects can influence the mechanical performance of the AM built part [3]. In this work, we describe a Configurable Additive Testbed (CAT) system used for laser powder bed fusion AM. The CAT system is a custom developed AM system that is comprised of an enclosed environmental chamber which has been modified to conduct laser powder bed fusion (LPBF) experiments [4,5]. The CAT is used to test various process parameters and materials and can be custom configured with a variety of sensors for in-situ NDE. We study the use of two high-speed, high-resolution cameras configured to image in the near infrared (NIR) band.

The NIR cameras are positioned in-line optically with the laser, and therefore the camera field of view follows the laser. The NIR cameras allow for high resolution imaging of the melt pool and surround areas. The thermal data is obtained during a laser melting process on a Ti-6Al-4V plate and of particular interest is the detection of keyhole porosity.

*joseph.n.zalameda@nasa.gov; phone 1 757-864-4793; fax 1 757-864-4914; http://nde.larc.nasa.gov

Keyhole porosity is a stochastic event and can result from certain build conditions, such as excessive laser power at a given. laser scanning speed and laser beam focus that creates a depression zone producing an entrapped bubble [6-9]. The NIR measured melt pool and cooling areas are processed to detect keyhole porosity. The results are compared to X-ray computed tomography (CT) results for validation.

2. ADDITIVE MANUFACTURING AND MEASUREMENT SYSTEM DESCRIPTION

2.1 Configurable Additive Testbed (CAT)

The CAT system is comprised of an enclosed environmental chamber that has been modified to conduct LPBF experiments with a variety of sensors and multiple view port windows for various camera configurations. Shown in Figures 1(a) and 1(b) are a picture of the CAT system and drawing respectively. The CAT is configured with an environmental chamber such that the builds are conducted with <10 ppm O_2, measured using a PureAire[1] trace oxygen analyzer. The crossflow velocity is measured to be 90 mm/s. A SCANLAB GmbH IntelliScan III 20[1] galvanometer head is driven by a SCANLAB RTC61[1] control board and an IPG Photonics[1] modulated continuous emission 1070 nm Gaussian laser with a maximum power of 1 kW to conduct the welds. A Jenoptik F-Theta[1] lens with a 255 mm working distance is used for a near uniform laser spot diameter of 40 µm across a 25.4 x 25.4 mm build area. The in-line (coaxial to the laser heat source) camera sensor setups are shown in Figure 2. The setup shows beam splitter #2 which splits the light for the two NIR cameras. Camera #1 is configured with a 725 nm bandpass filter with full width half max (FWHM) band pass from 700 to 750 nm. Camera #2 is configured with a 900 nm bandpass filter with FWHM band pass from 875 to 925 nm. Both camera fields of view follow the laser path using the SCANLAB GmbH[1] camera adapter that consists of a focusing objective (configured with 1070 nm notch filters) and a beam splitter #1. This coaxial method is used to obtain the highest resolution imagery of the melt process. The beam splitter #1 also separates the 1070 nm laser beam from NIR wavelengths that are measured by the cameras. The in-line cameras used are the Photron Fastcam Nova S6[1]. These cameras have a CMOS sensor, a 20 x 20 um pixel pitch, a 1024 x 1024 pixel array, a dynamic range of 12 bits, and a maximum frame rate of 6,400 Hz at full pixel resolution. The fields of view of the cameras are configured to capture 512 x 512 pixels and therefore a 10,000 Hz frame rate is used. The camera integration time was set to 10 us. The cameras are triggered simultaneously in concert with the mirror position and therefore the exact position of the laser is known within the camera imagery. The spectral sensitivity of the camera is shown in Figure 3a and Figure 3b shows the camera's filtered responses. As shown in Figure 3b camera #1 (725 nm filter) has over double the sensitivity as compared to camera #2 (900 nm filter).

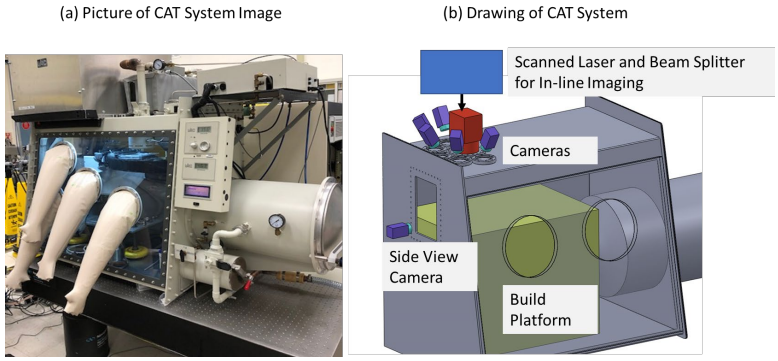

Figure 1: CAT system setup (a) picture of system and (b) drawing of test setup.

2.2 Estimation of Effective NIR Camera Radiance versus Blackbody Temperature

The coaxial NIR cameras estimated effective radiance were calculated using equation 1 slightly modified from Palmer [10]. It is important to note that other optical components within the optical path, such as the beam splitters #1 and #2,

[1] Specific vendor and manufacturer names are used only to accurately describe the test hardware or software. The use of vendor and manufacturer names does not constitute an official endorsement, either expressed or implied, by the National Aeronautics and Space Administration nor does it imply that the specified equipment or software is the best available.

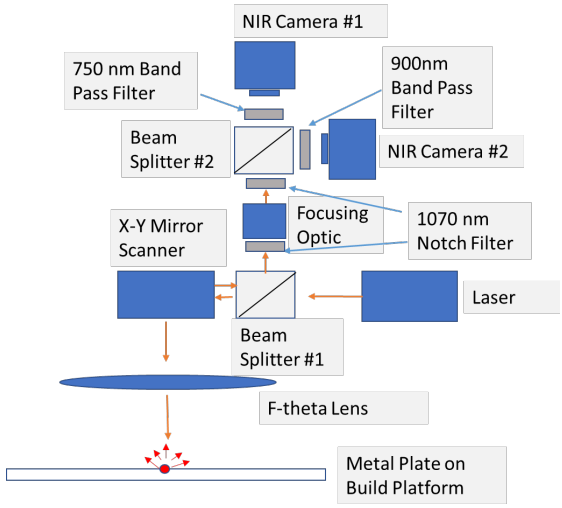

Figure 2: In-line NIR camera setup.

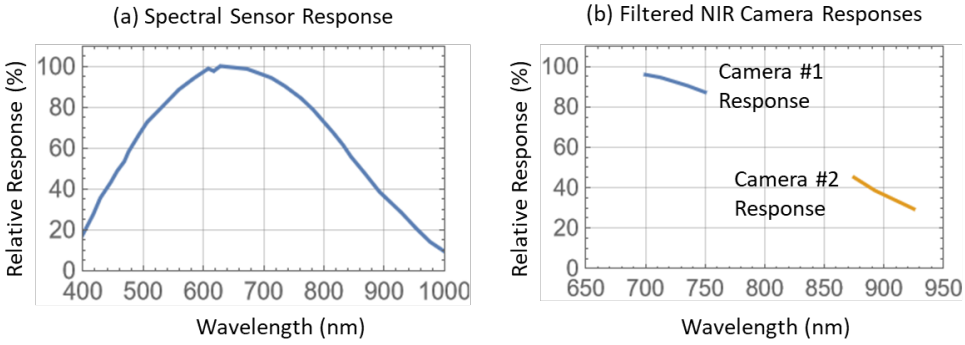

Figure 3: Overall camera spectral response and filtered responses.

mirror coatings, and focusing optics are not considered for these calculations. The sensor's response is included in equation (1) by linear interpolation of the sensor's relative response (Figure 3a) over the filter's wavelength band. The filters for the NIR cameras are modeled as "top hat" functions with 100% transmission in the passband.

$$Effective\ Band\ Radiance = \frac{1}{2}\int_{\lambda_1}^{\lambda_2} \frac{c_1}{\lambda^5\,\pi\,n^2\left(e^{\frac{c_2}{\lambda\,(T+273.15)}}-1\right)} * sensor(\lambda) * filter(\lambda) * d\lambda \quad (1)$$

For equation (1), λ is the wavelength variable, λ_1 and λ_2 is the wavelength bounds from 700 to 750 nm for camera #1 and 875 to 925 nm for camera #2. T is temperature in degrees Celsius. The effective in-band radiance is divided by 2 to account for the light split at beam splitter #2. The constants c_1 and c_2 values are 3.74177107 x 10^{20} watts nm^4/cm and 1.4387752 x 10^7 nm/Kelvin respectively. The index of refraction value in air is n = 1.00028. From equation (1) the blackbody temperature versus the effective radiance is calculated over a range of 800 to 2000 degrees Celsius as shown in Figure 4. As can be seen in Figure 4 there is more radiance energy for a given temperature from camera #1 as compared to camera number #2 for temperatures greater than 1650 degrees Celsius. Also, there is slightly more variation in the radiance values for camera #2 for temperatures less than 1650 degrees Celsius. This is expected since longer wavelengths allow for more sensitivity to relatively lower temperatures. For higher temperature measurements, camera #1 would be expected to have more sensitivity since the wavelength filter is in a shorter spectral band as compared to camera #2. For in-situ NDE applications during AM, it is beneficial to have more temperature sensitivity below the melt temperature for a given metal. The solidus temperature for Ti-6Al-4V is 1605 degrees Celsius [11]. Temperature sensitivity below this value is desired for in-situ thermal NDE and therefore it was expected that camera #2 would provide more signal at the lower temperatures. This was not the case as is discussed in the following section.

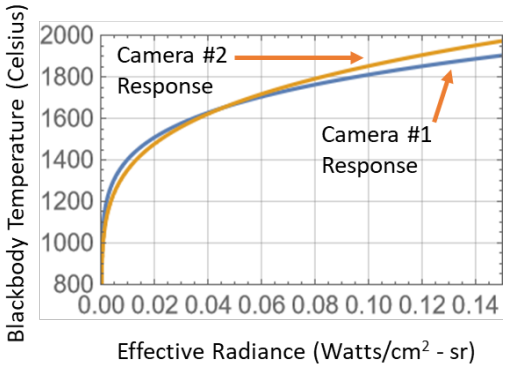

Figure 4: The blackbody temperature vs. in-band effective radiance response of the CAT NIR cameras.

3. MEASUREMENT RESULTS

3.1 CAT NIR Imaging of Ti-6Al-4V Plate

The laser was scanned at various powers and velocities to produce melting at the surface on a Ti-6Al-4V and thus creating the autogenous welds. Each weld line was approximately 1 cm in length. The processed plate top-down image with 270 total weld lines is shown in Figure 5. Also shown in Figure 5 are the main types of pore defects detected with X-ray CT (20-micron resolution per voxel). The X-ray CT images are averaged vertical slices taken along a given weld line. The pore defects consist of open pores, closed elongated pores, and small deep keyhole pores. The open pores at the end of the autogenous welds are rapidly solidified melt pools from the laser shut off. The closed elongated pores are produced by melt pool collapse and gas entrapment when the laser is shut off. The deep keyhole pores that occur along the autogenous welds are the result of unstable keyholes that are collapsing with gas entrapment while the laser is on.

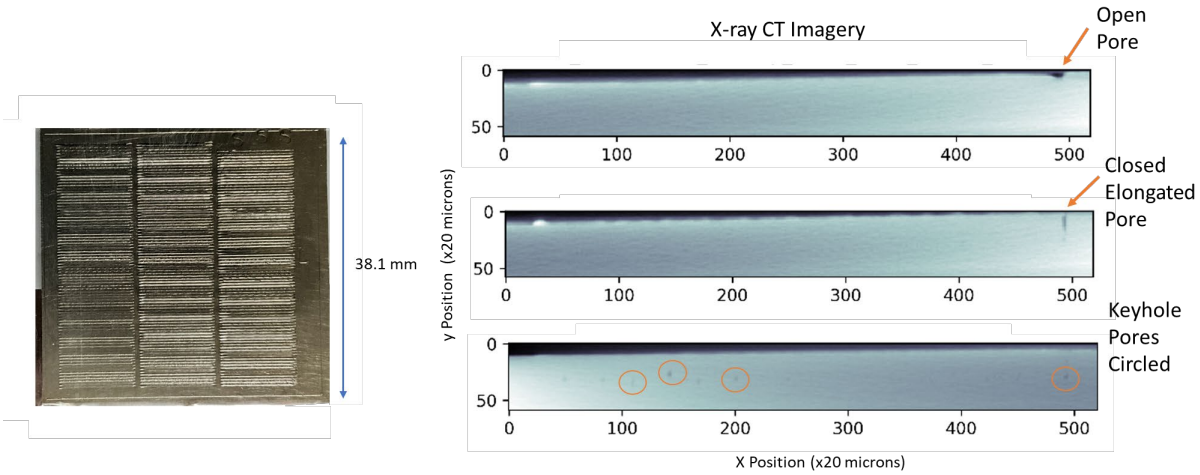

Figure 5: Top-down photograph of Ti-6Al-4V test plate showing the autogenous welds along with X-ray CT images of different pore defects.

The in-line NIR cameras were used to obtain imagery of the heating produced by the laser. Areas such as the metal melt pool and the transient cool down were observed using the NIR cameras. Shown in Figure 6a and 6b are representative images from the NIR cameras from both wave bands 700 – 750 nm and 875 – 925 nm respectively for a given weld with laser velocity of 1575 mm/sec and laser power of 366 watts. To simplify comparison, the NIR imagery were oriented in the same direction of laser travel. It is interesting to note the 700 – 750 nm band image had a significantly higher pixel intensity count as compared to the 875 – 925 nm NIR camera. This is most likely due to in-line optical path optics such as the mirrors, splitters, and focusing optics which suppressed the light in the longer waveband. Based on these findings, the NIR imagery from the shorter wavelength band (700 – 750 nm) camera #1 were analyzed further.

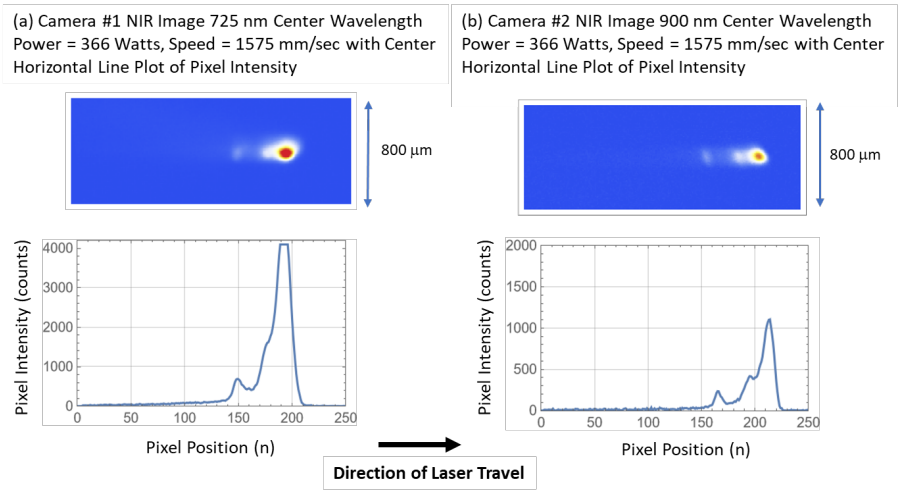

Figure 6: Example NIR camera imagery from camera #1(a) and camera #2(b) with corresponding line plots over the melt pool center.

3.2 NIR Camera Data Reconstruction

The NIR cameras are aligned co-axially with the laser and therefore the field of view followed the laser. The scanning velocity is recorded for a given laser spot position and acquired camera image. The camera resolution has been measured using a calibration target and was determined to be 7 microns/pixel. The camera imagery can then be reconstructed, for a known velocity, to produce a series of images that captures the laser generated melt pool along the entire scan track by overlaying each acquired image sequentially over a larger image which defines the scan track [12]. Each image represents the temperature versus time history. This allows aligning the maximum temperature for each pixel and this is shown in Figure 7. For each pixel the thermal decay can be measured and conventional thermal NDE algorithms can then be used to detect changes in the way the surface cools down. The camera frame rate is 10 kHz and therefore each reconstructed image represents a 0.0001 second time step. Defects can then be detected if the underlying substructure affects the surface cool down. For the timescales in this study, it is expected that near surface underlying defects would affect the cool down during melt pool solidification.

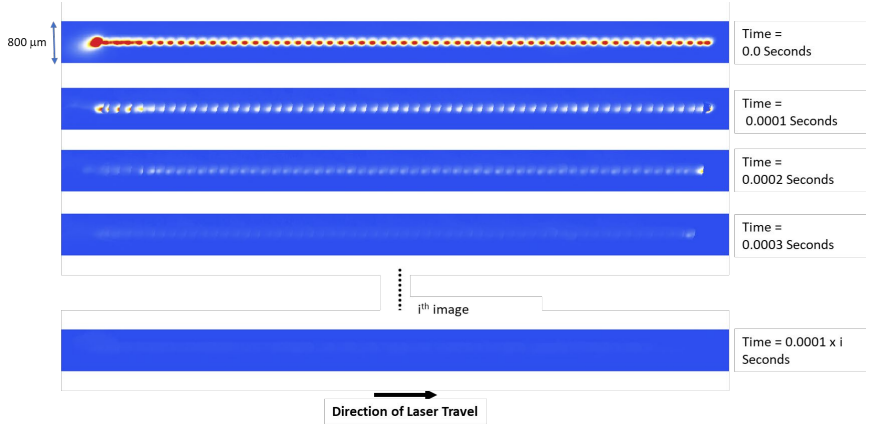

Figure 7: Reconstructed NIR camera #1 melt pool imaging for a given weld line with laser power = 366 watts, laser speed = 1575 mm/sec and camera frame rate of 10,000 Hz.

3.3 IR Camera Data Processing for Defect Detection

Principal component analysis (PCA) was used to detect defects in the reconstructed NIR thermal data [13]. PCA was used previously to analyze the thermal histories for keyhole porosity detection, however, the features detected did not correlate well with properties of interest in their study [14]. To facilitate comparison in this study, a fixed eigenvector approach was used wherein the covariance matrix for each data set (n) is averaged to produce a fixed eigenvector that is used to process all the data (N total data sets) [15]. The covariance matrix is computed for each data set by defining a

data matrix A_n, where the time variations are along the columns and the spatial image pixel points are row-wise. The matrix A_n is normalized by dividing by the maximum value and offset corrected by subtracting the mean along the time dimension. The *covariance matrix*$_n$ is defined as the $A_n{}^T A_n$. The *covariance matrix*$_n$ is now a square matrix of number of images used for processing and can then be averaged for all the total number of data sets (N). The averaged covariance matrix can then be decomposed using singular value decomposition to calculate the fixed eigenvectors.

$$\sum_{n=1}^{N} \frac{covariance\ matrix_n}{N} = \sum_{n=1}^{N} \frac{A_n^T A_n}{N} \tag{2}$$

The PCA inspection image is calculated by dot product multiplication of the selected fixed eigenvector times the temperature responses for each data set (data matrix A_n), pixel by pixel. The 1st eigenvector was used and appeared to provide good results over the 2nd eigenvector which produced more noisy images due to the limited time steps processed.

4. DATA ANALYSIS RESULTS

4.1 Fixed Eigenvector Imagery

A total of 25 weld lines were processed using the fixed eigenvector approach. The number of images selected for processing were 15 and this represents a time window of 0.0015 seconds. This time window includes the maximum temperature and subsequent cool down. This is sufficient time to capture the transition of molten metal to a solid-state. Any differences in how this transition occurs will allow for detection of defects since it is expected that solidification rates will be dependent on underlying structure [12]. A summary of the 25 weld line inspections is shown in Table 1 with highlighted lines representing false PCA indications or no PCA indication of shallow or open pore detected with X-ray CT. The deep keyhole pores (approximately deeper than 200 microns) were not detectable with this technique and therefore those weld line inspections were not highlighted. Representative PCA inspection results are shown in Figures 8 – 11 for weld #260 revealing a detected shallow elongated pore at end, weld #130 revealing a deep elongated pore not

Table 1: Summary of inspection results for 25 weld lines, highlighted welds represent PCA false indication or no PCA indication of shallow or open pore detected with X-ray CT.

Weld Number	Laser Power (watts)	Laser Speed 500-700 (mm/sec)	PCA Detected Anomaly	X-ray CT Porosity Inspection
67	244	599	Small Indication at End	Open Pore at End
79	244	598	No Indication	Small Deep Keyhole Pores
269	269	406	Indication at End	Open Pore at End
130	285	598	No Indication	Deep Small Pore at End
169	325	598	Indication at End	Open Pore at End
196	366	598	No Indication	Small Deep Keyhole Pores
243	407	598	No Indication	Small Deep Keyhole Pores
150	326	796	Small indication	Buried Shallow Pore at End
175	326	992	Indication at end	Small Deep Keyhole Pores, Nothing at End
192	367	795	No Indication	Open Pore at End
220	367	992	Indication at End	Buried Shallow Pore at End
262	407	794	No Indication	Deep Pore at End
266	407	794	Indication at end	Small Deep Keyhole Pores, No Pore at End
238	408	992	No Indication	Small Deep Keyhole Pores
47	203	1772	No Indication	No Pores
55	203	1773	Indication at end	Open Pore at End
152	326	1381	No Indication	Open Pore at End
210	365	1379	Small Indication at End	No Pores
197	366	1575	Indication at End	Open Pore at End
219	366	1575	Indication at End	Open Pore at End
199	366	1381	Indication at End	Open Pore at End
217	367	1578	Indication at Beginning and End	No Pores
267	406	1768	Indication at end	Small Pore at End
260	407	1186	Indication at end	Shallow Elongated Pore at End
246	408	1187	Indication at End	No Pores

detected, weld #169 revealing a detected open pore at the end, and weld #79 revealing small deeply buried keyhole pores (buried around 500 microns and deeper) not detected respectively. In Figures 8 – 11, the PCA images were displayed with a pixel intensity plot range of 0.8 – 1.15 and the PCA image threshold adjusted image was displayed using pixel intensity plot range values of 1.5 times the standard deviation plus the mean to 2.5 times the standard deviation plus the mean. All pixel intensity values below this range were colored green and all values above this range were colored red. The mean and standard deviation values were obtained by averaging 20 horizontal lines within the center of each PCA image. Those values are displayed in the middle line plots within Figures 8 – 11.

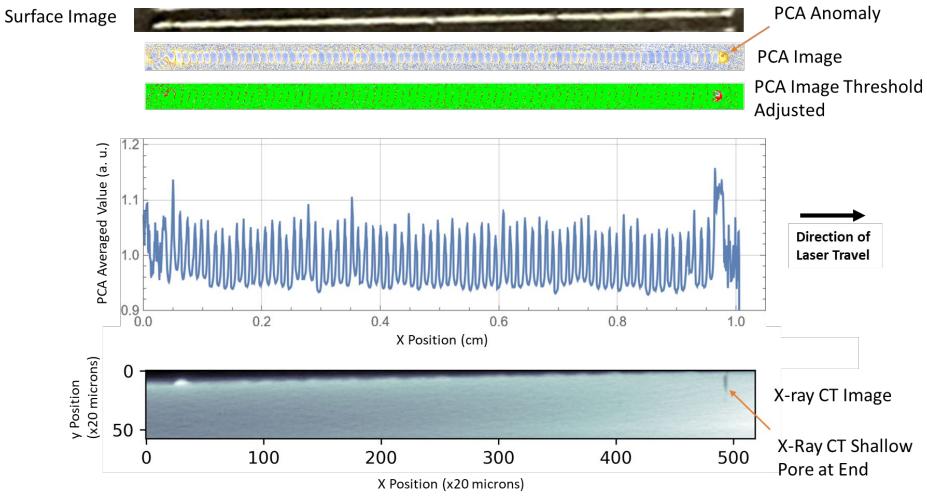

Figure 8: Weld #260 laser power = 407 watts, laser speed = 1186, mm/sec, shallow pore at end detected.

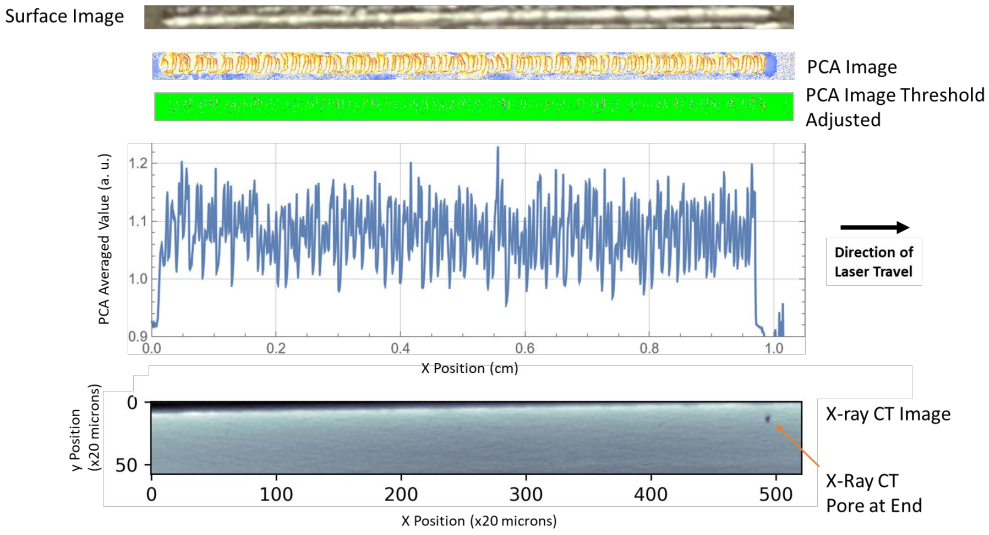

Figure 9: Weld #130 laser power = 285 watts, laser speed = 598, mm/sec, deep pore at end not detected.

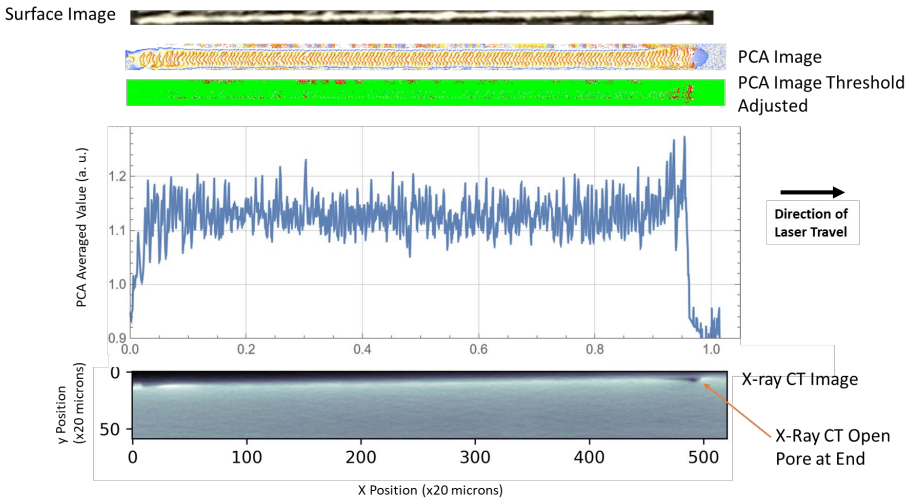

Figure 10: Weld #169 laser power = 325 watts, laser speed = 598, mm/sec, open pore at end detected.

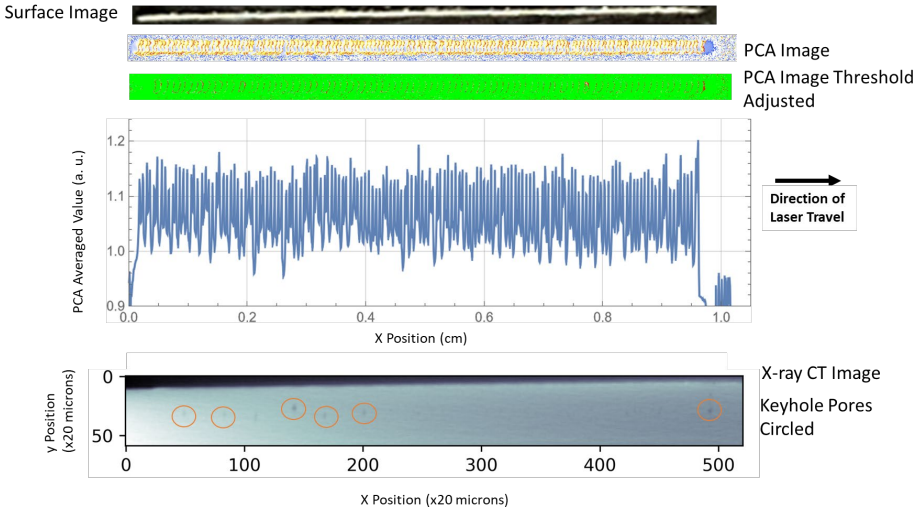

Figure 11: Weld #79 laser power = 244 watts, laser speed = 598, mm/sec, small keyhole pores not detected

5. CONCLUSIONS

As shown in Figure 11, small keyhole pores buried around 500 microns and deeper were not detectable using this in-situ inspection technique. Qualitatively some open pores or large pores buried near the surface (less than 200 microns) were detected, however, a thorough statistical analysis on more data sets will be required to establish feasibility and probability of detection since there were false indications as highlighted in Table 1. This technique perhaps may be more suited for lack of fusion porosity detection which can produce larger near surface pores. Also, efforts towards an automated data registration and comparison of the in-situ thermal measurements to the X-ray CT would be highly valuable since it is anticipated that processing of large data sets would be required for an AM build with many layers. Lastly, future investigation of modeling efforts will be necessary to further validate and optimize the inspection. Nevertheless, this inspection technique appears to have some potential for in-situ inspection during the AM building process.

ACKNOWLEDGEMENTS

This work was done under the NASA Aeronautics Research and Mission Directorate's Transformational Tools and Technologies (TTT) additive manufacturing project.

REFERENCES

[1] Yap, C.Y., Chua, C.K., Dong, Z.L., Liu, Z.H., Zhang, D.Q., Loh, L.E., and Sing, S.L., Review of Selective laser melting: Materials and applications, Applied Physics Reviews 2, 041101 (2015); doi:10.1063/1.4935926.

[2] Everton, S., Hirsch, M., Stravroulakis, P., Leach, R., and Clare, A., "A Review of in-situ process monitoring and in-situ metrology for metal additive manufacturing", AI, Materials & Design, vol. 95, April 2016.

[3] Soltani-Tehrani, A., Shrestha, R., Phan, N., Seifi, M., & Shamsaei, N. (2021). Establishing specimen property to part performance relationships for laser beam powder bed fusion additive manufacturing. International Journal of Fatigue, 151, 106384.

[4] Hocker, S.J.A., Richter, B., Spaeth, P.W., Kitahara, A.R., Zalameda, J.N., Glaessgen, E.H., 2023. A Point Field Driven Approach to Process Metrics Based on Laser Powder Bed Fusion Additive Manufacturing Models and In-Situ Process Monitoring. JMR. https://doi.org/10.1557/s43578-023-00953-7.

[5] Zalameda, J. N., Hocker, S. J., Fody J. M., Tayon, W. A., "Melt pool imaging using a configurable architecture additive testbed system", Proc. SPIE 11743, Thermosense: Thermal Infrared Applications XLIII, 117430E (12 April 2021); doi: 10.1117/12.2585791.

[6] Cunningham, R., Narra, S.P., Montgomery, C. et al. Synchrotron-Based X-ray Microtomography Characterization of the Effect of Processing Variables on Porosity Formation in Laser Power-Bed Additive Manufacturing of Ti-6Al-4V. JOM 69, 479–484 (2017). https://doi.org/10.1007/s11837-016-2234-1.

[7] Khairallah, S. A., Anderson, A. T., Rubenchik, A. and King, W. E., "Acta Materialia Laser powder-bed fusion additive manufacturing: Physics of complex melt flow and formation mechanisms of pores, spatter, and denudation zones," Acta Mater., vol. 108, pp. 36–45, 2016, doi: 10.1016/j.actamat.2016.02.014.

[8] Martin, A. A. et al. Dynamics of pore formation during laser powder bed fusion additive manufacturing. Nat. Commun. 10, 1987 (2019).

[9] Wang, L., Zhang, Y., Chia, H.Y. et al. Mechanism of keyhole pore formation in metal additive manufacturing. npj Comput Mater 8, 22 (2022). https://doi.org/10.1038/s41524-022-00699-6

[10] Palmer J M and Grant B G, The Art of Radiometry, vol PM184 SPIE Press Monograph (Bellingham, WA: 2010 SPIE Press).

[11] Solidus Temperature of Ti-6Al-4V,Titanium alpha-beta alloy, Grade 5 (Ti-6Al-4V) [SubsTech], accessed April 2024.

[12] Zalameda, Joseph N., Eric R. Burke, Robert A. Hafley, and Christopher S. Domack. "System and method for in-situ characterization and inspection of additive manufacturing deposits using transient infrared thermography." U.S. Patent 11,027,332, issued June 8, 2021.

[13] Rajic, N., "Principal Component Thermography for Flaw Contrast Enhancement and Flaw Depth Characterisation in Composite Structures", Composite Structures, Vol. 58, pp. 521--528, (2002).

[14] Paulson, N. H., Gould, B., Wolff, S. J., Stan, M., Greco, A. C., "Correlations between thermal history and keyhole porosity in laser powder bed fusion", Additive Manufacturing, Volume 34, 2020,101213, ISSN 2214-8604, https://doi.org/10.1016/j.addma.2020.101213.

[15] Cramer, K. E. and Winfree, W. P., "Fixed Eigenvector Analysis of Thermographic NDE Data", Proceedings of SPIE, Thermosense XXXIII, edited by Morteza Safai and Jeff Brown, Vol. 8013, (2011).